Advanced Powder Technology 22 (2011) 706–714

Contents lists available at ScienceDirect

Advanced Powder Technology

journal homepage: www.elsevier.com/locate/apt

Original Research Paper

Simulation and experimental studies of corona power loss in a dust loaded wire-duct electrostatic precipitator

Zakariya Al-Hamouz [a,*], Amer El-Hamouz [b], Nabil Abuzaid [c]

[a] Electrical Engineering Department, KFUPM, Dhahran 31261, Saudi Arabia
[b] Chemical Engineering Department, An Najah University, Nablus, Palestine
[c] Center for Water and Environment, RI, KFUPM, Dhahran 31261, Saudi Arabia

ARTICLE INFO

Article history:
Received 27 January 2010
Received in revised form 2 September 2010
Accepted 12 October 2010
Available online 26 October 2010

Keywords:
Electrostatics
Precipitators
Fly ash
Finite element
Method of characteristics corona

ABSTRACT

This paper investigates numerically and experimentally the performance of a single stage wire-duct electrostatic precipitators (WDEP) as influenced by different geometrical and operating parameters. To numerically solve the governing equations, namely Poisson's and the current continuity equations, the finite element method (FEM) and a modified method of characteristics (MMC) were used. One major advantage of the present work over those reported in the literature is that the characteristic lines follow the FE grid pattern which results in fast convergence and reduction of the computational time. To verify the results experimentally, a proto-type WDEP was successfully designed and fabricated at the research institute of KFUPM (RI-KFUPM). The experiments were carried out under laboratory conditions and a smoke of fired coal was used as a source of seed particles of PM10 category (around 78% of particles lying below 10 μm). The results show how different parameters (such as discharging wire radii's, wire-to-wire spacing and wire-to-plate spacing as well as the fly ash flow speed and applied voltage polarity) influenced the corona power loss and current density profiles. An indication of the effectiveness of this approach was carried out through a comparison of previously computed results and previously as well presently obtained experimental data.

1. Introduction

During this century, the world witnessed vast industrial and urban development, which affected positively the standard of life of human beings. However, enormous types of industrial wastes with tremendous quantities were generated as a side effect of this development. If not properly managed, these wastes would severely impact our environment. Particulate emissions are definitely among these industrial wastes that need control. Several systems and processes have been used for the control of particulate emissions. Those include settling chambers, cyclones, filters, wet scrubbers, and electrostatic precipitators (ESP). Although all systems share high collection efficiency, electrostatic precipitators are one of the most promising ways of controlling air pollution caused by industrial plants (smoke, fumes, and dust) [1,2].

The most common geometry of precipitators is the wire-duct or wire-plate electrostatic precipitator (WDEP) where a wide range of factors determine its performance [3,4]. For optimum design of WDEP, it is essential to determine the electric field, current density and hence the corona power loss and, finally, the collection efficiency. Theoretical as well as experimental analysis in WDEP has received the attention of several investigators. Many of the models reported depend on numerically solving the main system of equations with a certain choice of boundary conditions. Many investigators solved the governing equations with no dust loading conditions. For example, Butler et al. [5] interfaced the finite element method and the method of characteristics for solving the electric field and charge density values. Cooperman [6] presents a closed form analytic formula for predicting the current–voltage characteristics. For predicting the electric field and charge density under no dust loading conditions, Davis and Hoburg [7] combined the finite element method and the method of characteristics. On the other hand, Levin and Hoburg [8] used the finite element method and a donor cell method. Elmoursi and Castle [9] used the charge simulation method to model the electrical characteristics of wire-tube electrostatic precipitators. Their study involved the evaluation of the electric field, voltage and charge density distributions in the presence of mild corona quenching. Adamiak [10] predicted the characteristics of a WDEP by combining the method of characteristics and the boundary element method (BEM). Upwind (or downwind) finite difference scheme has been proposed by Lei et al. [11] for the calculation of the three-dimensional

* Corresponding author.
E-mail address: zhamouz@kfupm.edu.sa (Z. Al-Hamouz).

0921-8831/$ - see front matter © 2010 The Society of Powder Technology Japan. Published by Elsevier B.V. and The Society of Powder Technology Japan. All rights reserved.
doi:10.1016/j.apt.2010.10.005

Nomenclature

AOEC	study area of the WDEP
D	wire-to-wire spacing (m)
R	wire radius R (mm)
S	wire-to-plate spacing (m)
WDEP	wire-duct electrostatic precipitator
a	radius of assumed spherical particles (μm)
$A_{i,1}$	per unit cross-sectional area of the ith flux tube (m^2)
$\vec{E}$	electric field intensity vector (kV/m)
E_0	electric field on the discharging wire (kV/m)
e_r	a nodal potential error (−)
f	constant used in the particle charge density Eq. (9) (−)
g	an accelerating factor, taken to be equal to 0.5 (−)
I	corona current per unit length (μA/m)
(i,j)	finite element node made by the intersection of ith field line with jth equipotential contour
J_i	per-unit current density at the ith flux tube (μA/m^2)
$\vec{J}$	total current density vector (μA/m^2)
J_P	particle charge density values per unit length (μA/m^2)
k_{io}	mobilities for ions (m^2/V s)
k_p	mobilities for particles (m^2/V s)
$\vec{l}$	a unit vector along the axis of the flux tube (−)
M	number of flux tubes (−)
N	number of equipotential contours (−)
N_p	particle concentration per unit length (p/m^2)
S_p	particle's specific surface (m^2)
Δr_i	radial distance between the first two nodes along the axis of any flux tube
δ_1, δ_2	pre-specified percentage errors
ρ	total space-charge density per unit length (C/m^2)
ρ_{io}	ion charge density per unit length (C/m^2)
ρ_p	particle charge density per unit length (C/m^2)
φ	potential (kv)
ε_0	permittivity of free space (μF/m)
ε	relative permittivity (−)
γ	air viscosity (Pa s)
φ	potential within each finite element (kV)
φ_{av}	average value of the potential (kV)

distributions of the electric potential and the space charge in a wire-plate electrostatic precipitator. Numerical calculations based on the finite difference method and experimental investigations of gas-particle flows involving an electrical field, as they are found in the electrostatic precipitation process, has been reported by Böttner [12]. Under these dust free conditions, simultaneous solution for the governing Poisson's and current continuity equations of WDEP has been made by Rajanikanth and Thirumaran [13] using a combined boundary element and finite difference method over a one-quarter section of the precipitator. Anagnostopoulos and Bergeles [14] presented a numerical simulation methodology for the calculation of the electric field in wire-duct precipitation systems using finite differencing in orthogonal curvilinear coordinates to solve the potential equation. Neimarlija et al. [15] used the finite volume discretization of the solution domain as a numerical method for calculating the coupled electric and space-charge density fields in WDEP. An unstructured cell-centered second order finite volume method has been proposed for the computation of the electrical conditions by Long et al. [16]. On the other hand, under dust loading conditions, the equations governing the electrical conditions of cylindrical and wire duct precipitators have been solved using different numerical techniques. Elmoursi and Castle [17] succeeded in the use of the charge simulation method to model the electrical characteristics of cylindrical type electrostatic precipitators in the presence of dust loading. Abdel-Satar and Singer [18] presented a charge simulation numerical method for solving Poisson's equation, the current density equation and the current continuity equation in WDEP considering the effect of particle charge density and taking into account the effect of the variation of ion mobility with the ion position in space. Cristina and Feliziani [19] proposed a procedure for the numerical computation of the electric field and current density distributions in a "dc" electrostatic precipitator in the presence of dust, taking into account the particle-size distribution. Talaie [20] proposed a finite difference model for the prediction of electric field strength distribution and voltage–current characteristic for high-voltage wire-plate configuration. For particle of the size (0.1–0.1 μm), Ohyama et al. [21] proposed a finite difference numerical model for calculation the WDEP efficiency. For a cylinder wire plate electrode configuration, Dumitran et al. [22] estimated the electric field strength and ionic space-charge density. Talaie et al. [23] proposed a finite difference procedure to evaluate the voltage current characteristics in WDEP under positive and negative applied voltages. The model took the effect of particle charge into consideration and makes it possible to evaluate the rate of corona sheath radius augmentation as a result of increasing the applied voltage. Long et al. [24] used the unstructured finite volume method to compute the three-dimensional distributions of electric field and space-charge density. In computing the ionic space charge and electric field of WDEP, Beux et al. [25] proposed a semianalytical procedure, based on the Karhunen–Loeve (KL) decomposition to parameterize the current density field.

A group of experimental studies have been carried out under dust loading conditions. For example, Jedrusik et al. [26] investigated the influence of the physicochemical properties (chemical composition, particle-size distribution and resistivity) of the fly ash on the collection efficiency. For this purpose, three electrodes with a difference in design were tested. Miller et al. [27] investigated the impact of different electrode configurations on the WDEP efficiency. Zhuang et al. [28] presented experimental and theoretical studies for the performance of a cylindrical precipitator for the collection of ultra fine particles (0.05–0.5 μm). Measurements of the mass collection rates along a pilot WDEP in an industrial environment has been made by Bacchiega et al. [29].

In this paper, the performance of a proto-type WDEP has been investigated numerically under dust loading conditions (mainly the PM10 category). Different operating and geometrical parameters such as the applied voltage polarity, wire-to-wire spacing, wire-to-plate spacing, and wire radii are also investigated. The corona current, collecting (grounded) plates current density profiles as well as the corona power loss are computed and measured.

2. Mathematical formulation, assumptions and boundary conditions

2.1. Mathematical formulation

Fig. 1 shows a top view of a wire-duct electrostatic precipitator configuration. When the applied voltage is raised, the gas near the more sharply curved wire electrodes breaks down at a voltage above what is called the onset value and less than the spark breakdown value. This incomplete dielectric breakdown, which is called

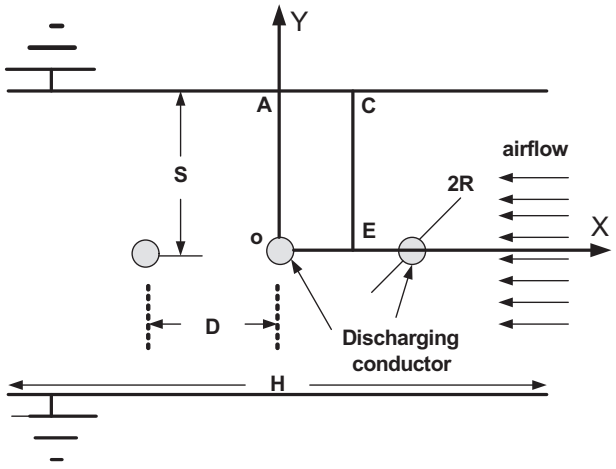

Fig. 1. Top view of a wire-duct electrostatic precipitator (WDEP).

a monopolar corona, appears in air as a highly active region of glow. The monopolar corona within duct-type precipitators includes only positive or negative ions (the back corona is neglected), the polarity of the ions being the same as the polarity of the high voltage wires in the corona. Due to the double symmetry in the precipitator geometry, Fig. 1, it is sufficient to study only the area AOEC (bounded by the points A, O, C, and E) for any number of corona wires, provided symmetry is preserved. In this figure, R is the wire (electrode) radius, S is the wire-to-plate spacing, D is the wire to wire spacing and H is the precipitator length.

For this configuration of WDEP, the following system of equations describes the monopolar corona:

$$\nabla \cdot \vec{E} = \rho/\varepsilon_0 \tag{1}$$

$$\nabla \cdot \vec{J} = 0 \tag{2}$$

$$\vec{E} = -\nabla\varphi \tag{3}$$

$$\vec{J} = \vec{J}_{io} + \vec{J}_p \tag{4}$$

$$\vec{J}_{io} = k_{io}\rho_{io}\vec{E} \tag{5}$$

$$\vec{J}_p = k_p\rho_p\vec{E} \tag{6}$$

where $\vec{E}$ is the electric field intensity vector, ρ is the total space-charge density (summation of the ion charge density ρ_{io} and particle charge density ρ_p, i.e. $\rho = \rho_{io} + \rho_p$), $\vec{J}$ is the total current density vector, φ is the potential, ε_0 is the permittivity of free space, and k_{io} and k_p are the mobilities for ions and particles, respectively.

Eqs. (1)–(6) represents Poisson's equation, the current continuity equation, the field and potential relation, the total current density equation, and the ion and particle current density equations, respectively. The exact analytical solution to these equations can only be obtained for parallel plates, coaxial cylinders and concentric spheres. Because of the nature of this problem, a numerical solution is anticipated as a tool for solving this set of equations. The following assumptions and boundary conditions are essential requirements for finding a numerical solution.

2.2. Simplifying assumptions

(1) The influence of particle space-charge density on the field may be approximated by assuming that the particle concentration N_p is constant over a given cross section of the precipitator. The particle's specific surface S_p (the surface per unit volume of gas) is given as [18]:

$$S_p = 4\Pi a^2 N_p \tag{7}$$

where a is the radius of assumed spherical particles.
The corona discharge is assumed to be distributed uniformly over the surface of the wires; if the corona electrode has a potential above a certain value, called the onset level, the normal component of the electric field remains constant at the onset value E_0, which results from Peek's derivation and later known as Kaptzov's assumption [30,31].

(2) The ion mobility is assumed constant.

(3) Ion diffusion is ignored.

2.3. Boundary conditions

(1) The potential at the two plates is zero.

(2) The potential at the discharging wires is V.

(3) The electric field at the discharging wires is E_0 which is given by [31]:

$$E_0 = 3.1 \times 10^6 \left(1 + \frac{0.308}{\sqrt{0.5 \times R}}\right) \tag{8}$$

3. Numerical procedure and experimental set-up

3.1. Proposed numerical procedure

Eqs. (1)–(6) which describe the WDEP are coupled partial differential equations (PDE_s). Therefore, one can solve the continuity equation if the electric field (or potential) is known and can solve Poisson's equation if the ionic space and/or particle charge density values are assumed known. Due to the double symmetry in Fig. 1, the boundary conditions $E_x = 0$ (electric field in the airflow direction) along the symmetry line O–A (where O is at the center of the corona wire) and $E_y = 0$ (electric field perpendicular to the airflow direction) along the symmetry line O–E (which is parallel to the grounded plates) are indirectly satisfied. Therefore, the solution algorithm consists of two coupled blocks: the FEM block and MMC block as shown in Fig. 2. The FEM block is used for solving Poisson's Eq. (1) to compute φ and E while the MMC block is used for solving the continuity Eq. (4) to compute the ionic space-charge density ρ_{io}.

The detailed steps of analysis are given hereafter.

3.1.1. Step 1: First FE grid generation

Generate a FE boundary fitted grid matched to the WDEP geometry as proposed before by Al-Hamouz [32]. The grid is generated from the intersection of field lines, which emanates from M nodes selected on the circumference of the discharging conductor, and N equipotential counters, Fig. 3.

The grid is made fine in the regions of high field gradient and becomes coarse in regions of low field gradients. After generating the free space charge FE grid, the electric field values at the FE nodes are determined from a third order interpolating polynomial of the potentials. Dividing each quadrilateral formed from the intersection of field lines with equipotential contours into two triangles, generates the triangular finite elements.

3.1.2. Step 2: Estimation of particle and ionic charge densities

Using the estimated electric field values on the FE grid nodes, the particle charge density ρ_p at each node is calculated from Eq. (9) [18]:

$$\rho_p = \varepsilon_0 f\, S_p\, E \tag{9}$$

where $f = 3$ for conducting particles and $f = 3\varepsilon/\varepsilon + 2$ for particles of relative permittivity ε. In other words;

$$\rho_p = \xi E \tag{10}$$

$$\xi = 4\Pi\varepsilon_0 f\, a^2 N_p \tag{11}$$

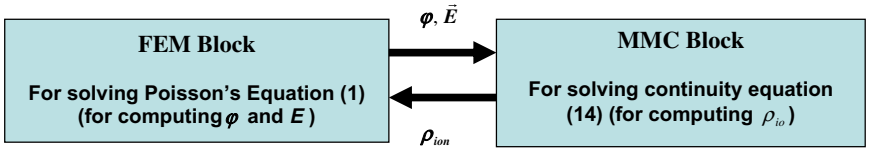

Fig. 2. FEM and the MMC coupling.

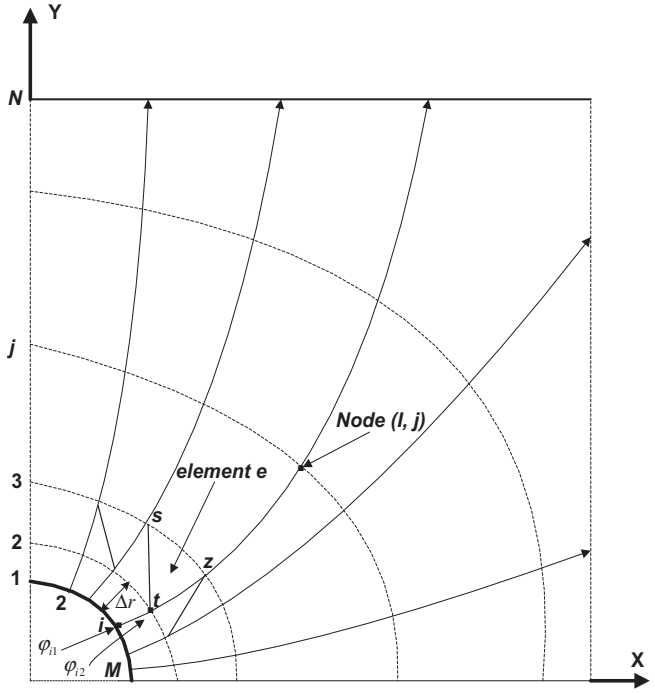

Fig. 3. Formation of triangular elements.

The particle mobility can be calculated as:

$$k_p = \rho_p / 6\Pi N_p \gamma a \tag{12}$$

where γ is the air viscosity.

The first estimate of the ionic space-charge density values at the FE grid nodes can be made by satisfying the current continuity equation, Eq. (2) using the MMC. The method of characteristics is based on a technique whereby the partial differential equation governing the evolution of charge density becomes an ordinary differential equation along specific "characteristic" space–time trajectories [9]. In the present work, a modified method of characteristics (MMC) is proposed where the partial differential equation governing the evolution of charge density becomes an ordinary differential equation along specific "flux tube" trajectories. Therefore, special flux tubes are introduced for this purpose, Fig. 3, which start at the surface of the discharging wire and terminate at the grounded plates. The ionic space charges are assumed to flow along the centers of these flux tubes, i.e. the field lines. Therefore, the problem that the characteristic lines never follow the FE grid pattern, which was reported previously by Adamiak [10], is eliminated in the present work.

$$\nabla \cdot \vec{J} = \nabla \cdot (k_{io}\rho_{io}E + k_p\rho_p E) = 0 \tag{13}$$

To simplify satisfying the continuity condition, particle charge density values $J_p = k_p\rho_p E$ are assumed constant in each iteration. Therefore, Eq. (13) has been simplified to solve for the ionic space-charge density values at the FE grid nodes. As a result, Eq. (13) can be written along each flux tube as:

$$\frac{d\rho_{io}}{dl}\bar{l} = -(\rho_{io}^2 + \rho_{io}\,\rho_p)/\varepsilon_0 E \tag{14}$$

where $\bar{l}$ is a unit vector along the axis of the flux tube, that is along the direction of E.

The initial estimate of the ionic space-charge density values on the circumference of the discharging electrode was assumed to follow the work in [32].

3.1.3. Step 3: Finite element solution of Poisson's equation

For known values of the ionic space charge and particle charge densities at the FE nodes, Poisson's equation, Eq. (1) is solved in the area AOEC by means of the FEM. The potential φ within each finite element is approximated as a linear function of coordinates [33], namely:

$$\varphi = \varphi^e W^e = \varphi_z w_z + \varphi_s w_s + \varphi_t w_t \tag{15}$$

with z, s, and t representing the nodes of the element e and W is the corresponding shape function. The constancy of the electric field at the discharging wire at a value of E_0 is directly implemented into the FE formulation. This is achieved by noting that $(\varphi_{i,1} - \varphi_{i,2})/\Delta r_i = E_0$ where Δr_i is the radial distance between the first two nodes along the axis of any flux tube, Fig. 2. Since $\varphi_{i,1}$ is the applied voltage, which is known, then $\varphi_{i,2}$, the potential at node (i,2), the ith node along the second equipotential contour, is also known and hence the boundary condition of constant electric field at the discharging wire is satisfied. It is worth mentioning, however, that Δr_i is much smaller than the discharging wire radius. Again, the electric field values at the FE nodes are determined from a third order interpolating polynomial of the potentials.

3.1.4. Step 4: Particle and space-charge density correction

Using the estimated electric field values at the FE nodes, the particle charge density at these nodes is updated using Eqs. (9)–(12). On the other hand, correction of the ionic space-charge density is made by comparing the computed values of the potential at the kth node in iterations n and $n+1$. A nodal potential error, e_r relative to the average value of the potential, φ_{av}, at that node is estimated. If the maximum of e_r along the axis of the ith flux tube exceeds a pre-specified value δ_1, a correction of the ionic space-charge density values $\rho_{i,1(io)}$ (corresponding to the ith flux tube) is made according to the maximum nodal error, as in Eq. (16):

$$\rho_{i,1(io)_{new}} = \rho_{i,1(io)_{old}}[1 + g\,F_k] \quad i = 1, 2, \ldots, M \tag{16a}$$

$$e_r = |\varphi_k^n - \varphi_k^{n+1}|/\varphi_{av} \tag{16b}$$

where

$$\varphi_{av} = (\varphi_k^n + \varphi_k^{n+1})/2 \tag{16c}$$

$$F_k = Maximum\,[(\varphi_k^{n+1} - \varphi_k^n)/\varphi_{av}] \tag{16d}$$

where g is an accelerating factor, taken to be equal to 0.5 and M is the number of flux tubes. The ionic space-charge density values at the rest of the FE nodes are estimated again by solving Eq. (14).

3.1.5. Step 5: Iteration to converge to a self-consistent solution

Steps 2–4 are repeated until the maximum nodal potential error of Eq. (16b) is less than a pre-specified value, δ_1.

3.1.6. Step 6: Next FE grid generation

The finite element grid is regenerated taking into account the latest nodal ionic, ρ_{io} and particle space charge values ρ_p until a self-consistent solution is obtained again for φ.

This process of grid generation and obtaining self-consistent solutions for φ and ρ continues until, for the last two generations, the maximum difference of the ionic space-charge density ρ_{io} at the FE nodes is less than a pre-specified value (δ_2 taken as 0.1% in the present work).

3.1.7. Step 7: Computation of corona current and corona power loss

For the whole discharging wire, the corona current is calculated as:

$$I = 4\sum_{i=1}^{M} J_i A_{i,1} \tag{17}$$

where J_i is the per-unit current density at the ith flux tube, and $A_{i,1}$ is the corresponding per unit cross-sectional area. The corona power loss per meter is the multiplication of the applied voltage by the corresponding corona current per meter.

In summary, the method of analysis is shown the flowchart of Fig. 4:

3.2. Proto-type experimental set-up

A one stage, dry type, parallel plate electrostatic precipitator was designed and fabricated at the High Voltage Laboratory, RI, King Fahd University of Petroleum and Minerals. The set-up top view is shown in Fig. 5.

The set-up consisted of a high voltage source (up to ±100 kV), and dust particle feeder and blower. The single stage WDEP model is made of two collection plates (2 m × 1 m), one of the plates is covered by 35 aluminum strips (1 m × 5 cm) separated by 3 mm, while the other plate is covered by a complete aluminum plate. This arrangement makes it possible to measure the grounded plate current density profile. In order to measure the current density at each strip, holes were made through each strip, nails were placed

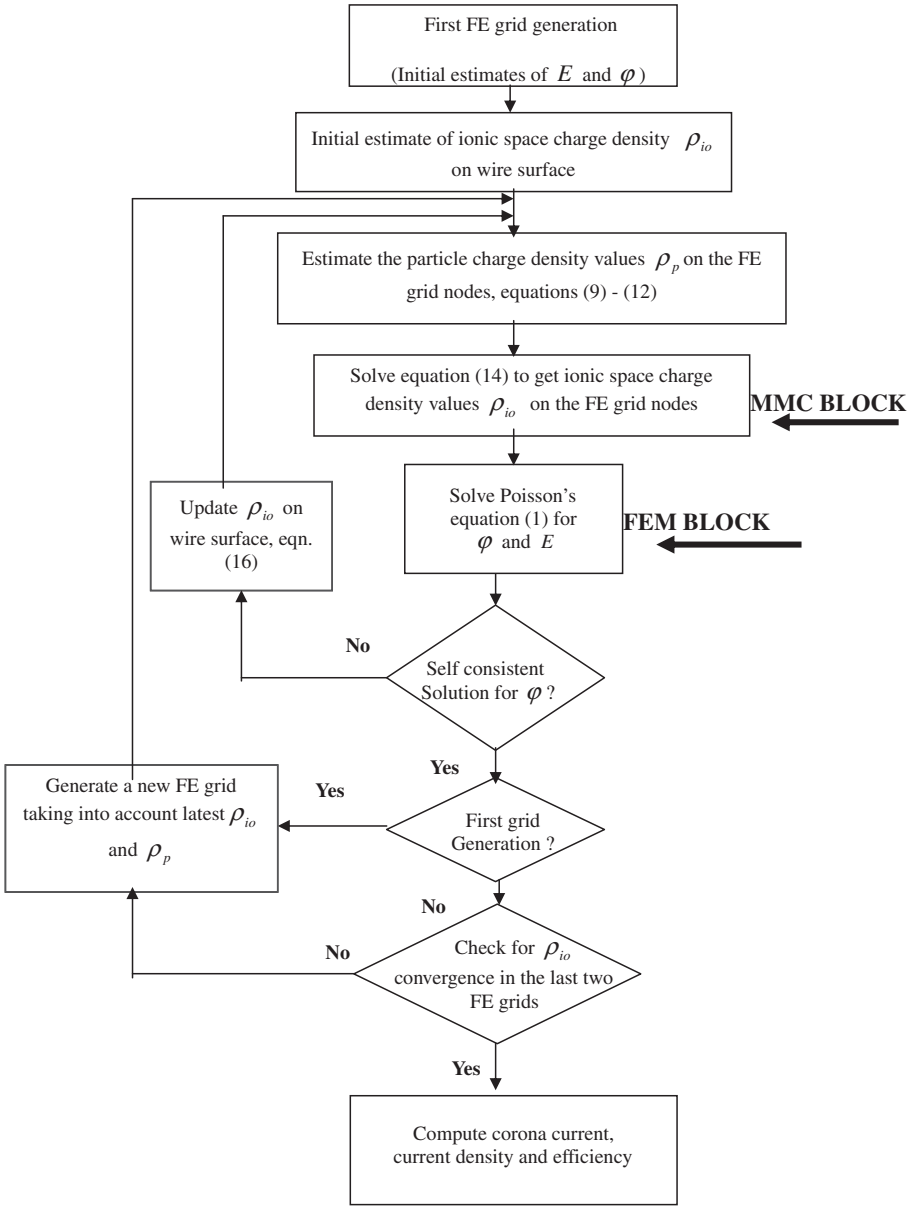

Fig. 4. Solution flowchart.

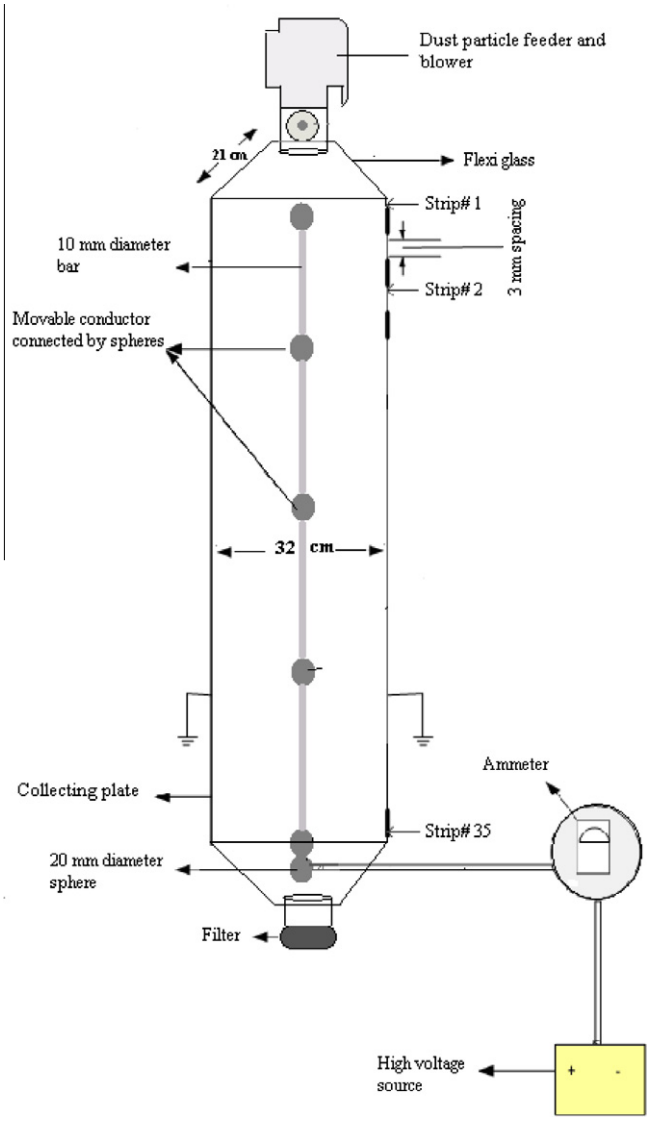

Fig. 5. Top view of the fabricated experimental set-up.

through the holes and wires were connected between the nails and the current measuring board. The experimental set-up has the feature of changing the plate-to-plate spacing, and the discharging wire-to-wire spacing. The voltage source is connected to a conductor rod hanging horizontally to the rooftop.

4. Numerical and experimental results

4.1. Comparison with previous experimental and numerical findings

The configuration reported in [14,34], where cement dust particles having a dominant particle radius of 30 μm, has been used to test the effectiveness of the computational algorithm. For this WDEP model, the discharging wire radius R is 0.521 mm, wire-to-plate spacing S is 101.6 mm, and wire-to-wire spacing D is 203.2 mm. The method of analysis generates 526 finite element nodes and converges in three grid generations each with seven iterations. The present calculated corona power loss compared to the previously measured [34] and calculated [14] values is shown in Fig. 6. The present agreement with experimental findings is better than that of [14].

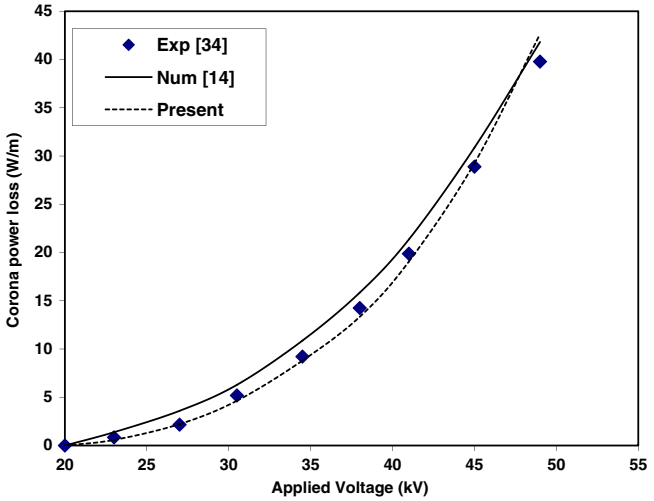

Fig. 6. Comparison between computed and experimental power loss characteristics (R = 0.521 mm, wire to plate S = spacing = 101.6 mm, wire to wire spacing D = 203.2 mm).

For another configuration with a discharging wire radius R of 0.204 mm, wire-to-wire spacing D of 50 mm, wire-to-plate spacing S of 25 mm and a positive applied voltage of 15 kV, the previously calculated [35] and measured [36] collecting plate current density profiles as compared to the presently calculated values are shown in Fig. 7. Again, it is clear that the present computed results are in better agreement with experimental values.

4.2. Comparison with present experimental and numerical findings

Using the fabricated experimental set-up, the present computational algorithm values are compared to the measured corona power loss and current density profiles. The basic geometrical and operating parameters used are listed in Table 1.

4.2.1. Corona power loss

4.2.1.1. Effect of varying the applied voltage polarity. The effect of varying the polarity of the applied voltage on the measured and numerically calculated corona power loss characteristics is shown in Fig. 8. The agreement between the computed and experimental values is satisfactory. As can be seen, for a certain applied voltage,

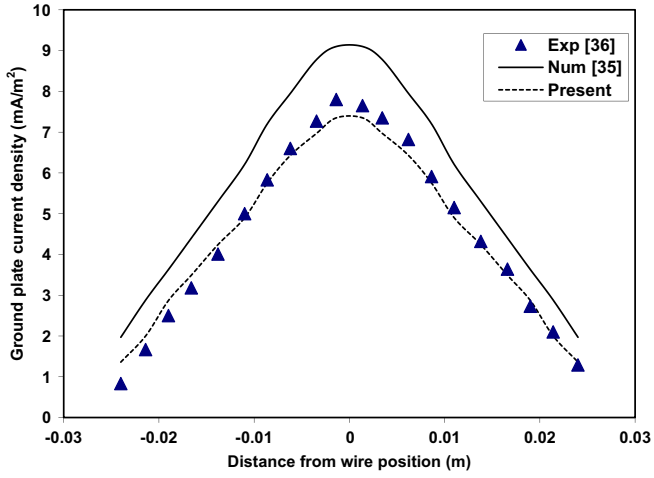

Fig. 7. Ground plate current density profile (+ve 15 kV applied voltage, R = 0.204 mm).

Table 1
Geometry and operating parameters of the laboratory set-up.

Parameter	Value
Length of collection plate (ESP length in m)	2
Height of collection plate (ESP height in m)	1
Spacing between collecting and discharging electrode (m)	0.3 and 0.4
Spacing between discharging electrodes (m)	0.16 and 0.21
Radii's of discharging electrodes (mm)	0.35, 0.5, 0.85
Air flow velocity (m/s)	0.5–2.2
Atmospheric pressure (Pa)	1
Ion mobility ($m^2/V\,s$)	1.82×10^{-4}
Supply Voltage (kV)	0–100
Temperature of gas (K)	293

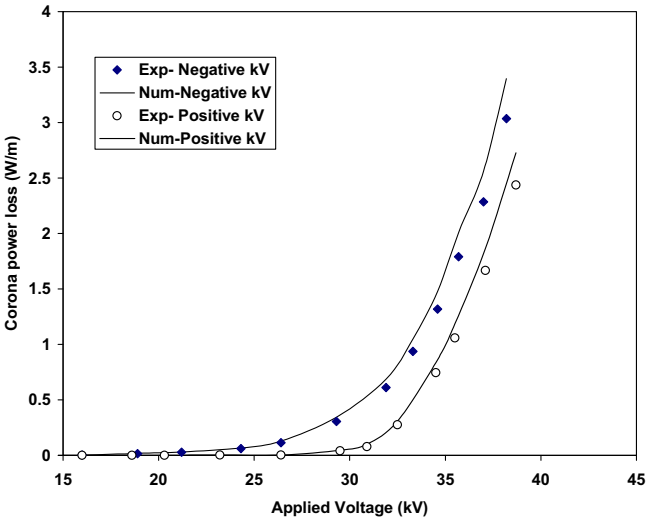

Fig. 8. Effect of varying applied voltage polarity on corona power loss (D = 0.3 m, S = 0.21 m, R = 0.85 mm).

the corona power loss and hence the value of corona current is higher for negative applied voltage as compared to the values when the same amount of positive voltage is applied. Therefore, negative applied voltage is used for all present experimental and numerical investigations.

4.2.1.2. Effect of discharging wire radii. In order to investigate the effect of varying the discharging wire radii, wires with three different radii's, namely 0.35, 0.5 and 0.85 mm, were used. The presently measured and calculated corona power loss characteristics for the three cases are shown in Fig. 9. The agreement between the calculated and measured findings is quite acceptable. Also, it can be seen that as the wire radius increases, the corona power loss decreases. This can be easily attributed to the fact that as the wire radius increases, the corona onset voltage increases and subsequently the corona current decreases for the same applied voltage.

4.2.1.3. Effect of varying discharging wire-to-wire spacing (D). The effect of varying the discharging wire-to-wire spacing (D), while keeping the discharging wire radius and wire-to-plate spacing fixed is investigated. The presently measured and calculated corona power loss characteristics for wire-to-wire spacing of 0.3 and 0.4 m are in good agreement and are shown in Fig. 10. It is quite interesting to notice that, for a constant discharging wire radius and constant wire-to-plate spacing, the corona power loss increases as the wire-to-wire spacing increases while keeping the voltage constant. This is attributed to the mutual effect among

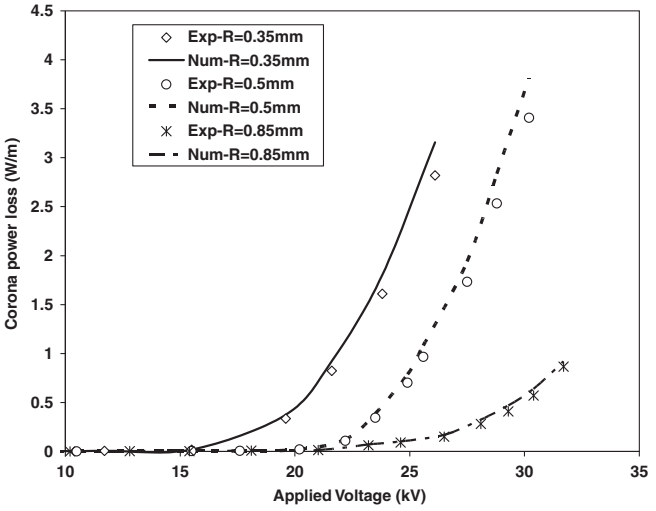

Fig. 9. Effect of varying discharging wire radii's on corona power loss (S = 0.16 m, D = 0.3 m).

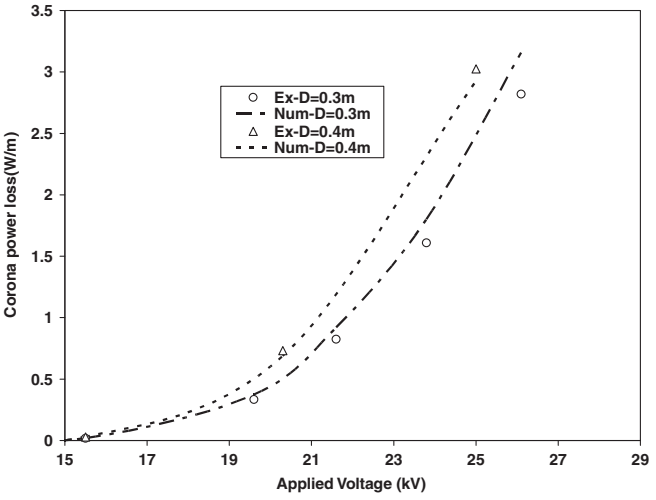

Fig. 10. Effect of varying discharging wire-to-wire spacing on corona power loss (S = 0.16 m, R = 0.35 mm).

the discharge wires where each wire (except the wires at the ends) is shielded by the surrounding two wires. Such shielding results in compacting the field lines over the wire surface. The larger the distance between wires, the less is the compactness of the field lines and the larger is the area on the wire surface where field lines emanates. Therefore, the corona current per wire and hence the total corona current increases with the increase of the wire-to-wire spacing.

4.2.1.4. Effect of varying discharging wire-to-plate spacing (S). The effect of varying the discharging wire-to-plate spacing (S), while keeping the discharging wire radius and wire-to-wire spacing fixed is investigated. The presently measured and calculated corona power loss characteristics for wire-to-plate spacing of 0.16 and 0.21 m are in good agreement and are shown in Fig. 11. It can be seen that, at the same applied voltage, the corona power loss increases as the wire-to-plate spacing decreases. This is attributed to the fact that as the wire-to-plate spacing decreases, the corona onset voltage decreases.

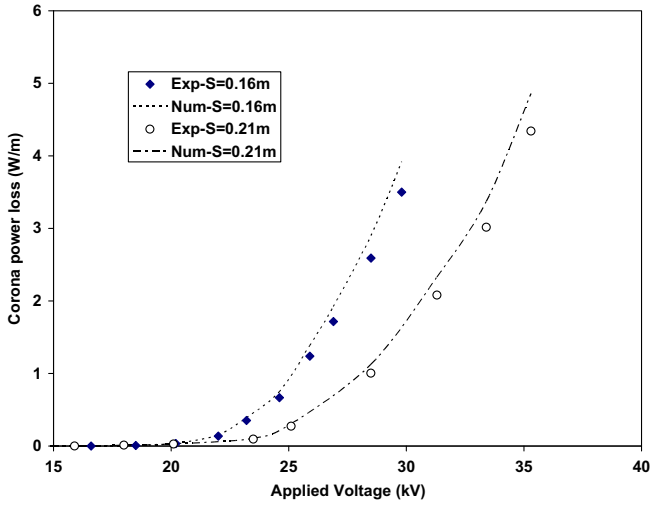

Fig. 11. Effect of varying discharging wire-to-plate spacing on corona power loss (D = 0.4 m, R = 0.5 mm).

4.2.2. Ground plate current density profiles

For one of the configurations tested in Fig. 10, namely for a WDEP with wire-to-plate spacing S of 0.16 m, discharging wire radii R of 0.85 mm, and an applied voltage of −31.5 kV, the present measured and calculated ground plate current density profiles for two wire-to wire spacing (D = 0.3 and 0.4 m) is shown in Fig. 12. The results show good agreement between the presently measured and computed values. It can also be noted that as the wire-to wire spacing increases, the maximum values of the current density profiles increases. This is a consequence of the reduction in the corona onset voltage. It is also worth noting that the maximum current density value under the central discharging wire is less than the other two wires. This is attributed to the mutual effect among the discharge wires where each wire (except the wires at the ends) is shielded by the surrounding two wires.

4.3. Accuracy, simplicity, and computational time

It is quite clear from Figs. 6 and 7 that the calculated values predicted by the present algorithm are in better agreement with experimental results than previous attempts reported in the literature. In addition, and contrary to one main problem reported in the literature, the FE grid is generated in a simple way where the characteristic lines follow the FE grid pattern. This will, in effect, reduce the number of FE grid re-generations needed to achieve convergence. Also, the previous methods [10,18] call in their programming for two inner loops to guarantee convergence, one for the convergence of the potential and the other for the convergence of electric field to the onset value. An outer loop to update the mapped field lines (i.e. the FE grid) is also required, which means that a total of three loops are needed for convergence of the previous methods. On the other hand, the present algorithm requires only one loop to guarantee the convergence of the potential, and one loop to update the FE grid. Hence a total of two loops is needed to guarantee convergence. For example, for one of the configurations, the present algorithm requires two grid generations and five iterations (a total of 10 iterations) to convergence with an accuracy of 0.1% in the computed results. On the other hand, in [18], the total number of iterations needed for conversion is 15–28 with an accuracy of less than 1% in the computed results. This reduction in the number of iterations is attributed to the fact that the FE grid is generated from the intersection of field lines and equipotential contours Unfortunately, the authors in [14,35] did not report the number of iterations needed for conversion.

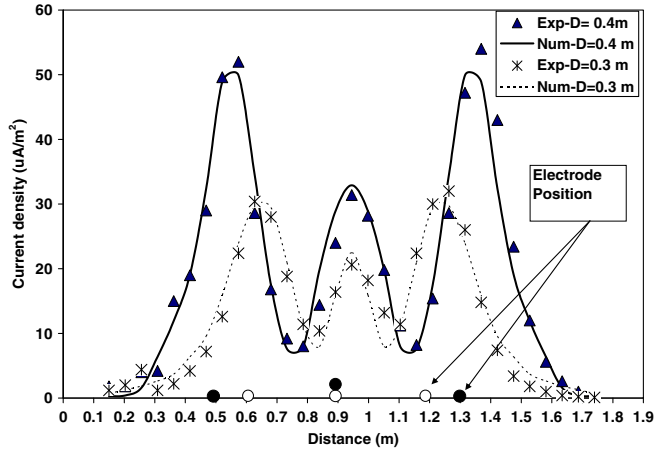

Fig. 12. Present calculated and measured ground plate current density distribution (S = 0.16 m, R = 0.85 mm, V = −31.5 kV).

5. Conclusions

A combined finite element based method (FEM) and a modified method of characteristics (MMC) is developed for the analysis and computation of space-charge density, corona current and hence power loss associated with WDEP. One major advantage of the present work over those reported in the literature is that the characteristic lines follow the FE grid pattern. To test the developed algorithm, comparison with experimental and numerical findings reported in the literature has been made where the present algorithm showed high accuracy accompanied with a reduction in the number of iterations needed to converge. The results show how different design parameters (such as discharging wire radii's, wire-to-wire spacing and wire-to-plate spacing and applied voltage polarity) influenced the corona current and current density profiles.

Acknowledgment

The authors thank King Fahd University of Petroleum and Minerals for the financial support of this work under Project No. SB 08-019.

References

[1] Alexandru Artino, Mircea Cârdu, Electrostatic precipitators used in the ecological conversion of power in coal-fired thermoelectric power plants, Energy Conversion and Management 35 (1994) 477–481.
[2] R. Macarie, D. Martin, New technologies for the electrostatic precipitators pulsed energization in energetics, Energy Conversion and Management 38 (1997) 511–516.
[3] M. Robinson, Electrostatic precipitation, in: W. Strauss (Ed.), Air Pollution Control, Wiely-Interscience, 1971.
[4] H.E. Rose, A.J. Wood, An Introduction to Electrostatic Precipitators, second ed., London, Constable, 1966.
[5] A. Butler, Z. Cendes, J. Hoburg, Interfacing the finite-element method with the method of characteristics in self-consistent electrostatic field models, IEEE Transactions on Industry Applications 25 (1989) 533–538.
[6] G. Cooperman, A new current–voltage relation for duct precipitators valid for low and high current densities, IEEE Transactions on Industry Applications 17 (1981) 236–239.
[7] J. Davis, J. Hoburg, Wire-duct precipitator field and charge co using finite element and characteristics methods, Journal of Electrostatics 14 (1983) 187–199.
[8] P. Levin, J. Hoburg, Donor cell-finite element descriptions of wire-duct precipitator fields, charges, and efficiencies, IEEE Transactions on Industry Applications 26 (1990) 662–670.

[9] A.A. Elmoursi, G.S. Castle, Modeling of corona characteristics in a wire-duct precipitator using the charge simulation method, IEEE Transactions on Industry Applications 23 (1987) 95–102.
[10] K. Adamiak, Simulation of corona in wire-duct electrostatic by means of the boundary element method, IEEE Transactions on Industry Applications 30 (1994) 381–386.
[11] Hong Lei, Lian-Ze Wang, Zi-Niu Wu, Applications of upwind and downwind schemes for calculating electrical conditions in a wire-plate electrostatic precipitator, Journal of Computational Physics (2004) 697–707.
[12] C.-U. Böttner, The role of the space charge density in particulate processes in the example of the electrostatic precipitator, Powder Technology (2003) 285–294.
[13] B.S. Rajanikanth, N. Thirumaran, Prediction of pre-breakdown V–I characteristics of an electrostatic precipitator using a combined boundary element-finite difference approach, Fuel Processing Technology (2002) 159–186.
[14] J. Anagnostopoulos, G. Bergeles, Corona discharge simulation in wire-duct electrostatic precipitator, Journal of Electrostatics (2002) 129–147.
[15] N. Neimarlija, I. Demirdzic, S. Muzaferija, Finite volume method for calculation of electrostatic fields in electrostatic precipitators, Journal of Electrostatics (2009) 37–47.
[16] Z. Long, Q. Yao, Q. Song, S. Li, A second-order accurate finite volume method for the computation of electrical conditions inside a wire-plate electrostatic precipitator on unstructured meshes, Journal of Electrostatics (2009) 597–604.
[17] A.A. Elmoursi, G.S. Castle, The analysis of corona quenching in cylindrical precipitators using charge simulation, IEEE Transactions on Industry Applications 22 (1986) 80–85.
[18] S. Abdel-Satar, H. Singer, Electrical conditions in wire-duct electrostatic precipitators, Journal of Electrostatics 26 (1991) 1–20.
[19] S. Cristina, M. Feliziani, Calculation of ionized fields in DC electrostatic precipitators in the presence of dust and electric wind, IEEE Transactions on Industry Applications 31 (1995) 1446–1451.
[20] M.R. Talaie, Mathematical modeling of wire-duct single-stage electrostatic precipitators, Journal of Hazardous Materials B 124 (2005) 44–52.
[21] R. Ohyama, K. Urashima, J. Chang, Numerical modeling of wire-plate electrostatic precipitator for control of submicron and ultra fine particles, Journal of Aerosol Sciences (2000) S162–S163.
[22] L. Dumitran, L. Dascalescu, P. Notingher, P. Atten, Modelling of corona discharge in cylinder-wire-plate electrode configuration, Journal of Electrostatics (2007) 758–763.
[23] M. Talaie, M. Taheri, J. Fathikaljahi, A new method to evaluate the voltage–current characteristics applicable for a single-stage electrostatic precipitator, Journal of Electrostatics (2001) 221–233.
[24] Z. Long, Q. Yao, Q. Song, S. Li, Three-dimensional simulation of electric field and space charge in the advanced hybrid particulate collector, Journal of Electrostatics (2009), doi:10.1016/j.elstat.2009.07.001.
[25] F. Beux, A. Iollo, M. Salvetti, A. Soldati, Approximation and reconstruction of the electrostatic field in wire-plate precipitators by a low-order model, Journal of Computational Physics (2001) 893–916.
[26] Maria Jedrusik, Arkadiusz Swierczok, Ryszard Teisseyre, Experimental study of fly ash precipitation in a model electrostatic precipitator with discharge electrodes of different design, Powder Technology (2003) 295–301.
[27] J. Miller, B. Hoferer, A. Schwab, The impact of corona electrode configuration on electrostatic precipitator performance, Journal of Electrostatics (1998) 67–75.
[28] Y. Zhuang, Y. Kim, T. Lee, P. Biswas, Experimental and theoretical studies of ultra-fine particle behavior in electrostatic precipitators, Journal of Electrostatics (2000) 245–260.
[29] G. Bacchiega, I. Gallimberti, E. Sani, R. Sala, V. Ar rondel, M. Hamlil, E. Christensen, Experimental study of the mass balance in a pilot industrial electrostatic precipitator, Journal of Electrostatics (2006) 297–309.
[30] N. Kaptzov, Elektricheskie Invlentiia v Gazakh I Vakuu mme, Ogiz, Moscow, U.S.S.R., 1947, pp. 587–630.
[31] F. Peek, Determination Phenomena in High Voltage Engineering, McGraw-Hill, New York, 1929, pp. 52–80.
[32] Z. Al-Hamouz, A combined algorithm based on finite elements and modified method of characteristics for the analysis of corona in wire-duct electrostatic precipitators, IEEE Transactions on Industry Applications 38 (2002) 43–49.
[33] L. Segerlind, Applied Finite Element Analysis, Wiley, New York, 1984.
[34] N.J. Felici, Recent Advances in the Analysis of the dc Ionized Fields – Part II, Direct Current, vol. 8, 1963, pp. 278–287.
[35] K.S.P. Nikas, A.A. Varonos, G.C. Bergeles, Numerical simulation of the flow and the collection mechanisms inside a laboratory scale electrostatic precipitator, Journal of Electrostatics (2005) 423–443.
[36] N. Parasram, Particle Motion in Electrostatic Precipitators, Ph.D. Thesis, Mechanical Engineering Department, Imperial College of Science, Technology and Medicine, 2001.